

Nanoscale mapping of contact stiffness and damping by contact resonance atomic force microscopy

This article has been downloaded from IOPscience. Please scroll down to see the full text article.

2012 Nanotechnology 23 215703

(<http://iopscience.iop.org/0957-4484/23/21/215703>)

View [the table of contents for this issue](#), or go to the [journal homepage](#) for more

Download details:

IP Address: 129.6.130.14

The article was downloaded on 04/05/2012 at 13:32

Please note that [terms and conditions apply](#).

Nanoscale mapping of contact stiffness and damping by contact resonance atomic force microscopy

Gheorghe Stan¹, Sean W King² and Robert F Cook¹

¹ Nanomechanical Properties Group, National Institute of Standards and Technology, Gaithersburg, MD 20899, USA

² Portland Technology Development, Intel Corporation, Hillsboro, OR 97124, USA

E-mail: gheorghe.stan@nist.gov

Received 14 February 2012

Published 3 May 2012

Online at stacks.iop.org/Nano/23/215703

Abstract

In this work, a new procedure is demonstrated to retrieve the conservative and dissipative contributions to contact resonance atomic force microscopy (CR-AFM) measurements from the contact resonance frequency and resonance amplitude. By simultaneously tracking the CR-AFM frequency and amplitude during contact AFM scanning, the contact stiffness and damping were mapped with nanoscale resolution on copper (Cu) interconnects and low-*k* dielectric materials. A detailed surface mechanical characterization of the two materials and their interfaces was performed in terms of elastic moduli and contact damping coefficients by considering the system dynamics and included contact mechanics. Using Cu as a reference material, the CR-AFM measurements on the patterned structures showed a significant increase in the elastic modulus of the low-*k* dielectric material compared with that of a blanket pristine film. Such an increase in the elastic modulus suggests an enhancement in the densification of low-*k* dielectric films during patterning. In addition, the subsurface response of the materials was investigated in load-dependent CR-AFM point measurements and in this way a depth dimension was added to the common CR-AFM surface characterization. With the new proposed measurement procedure and analysis, the present investigation provides new insights into characterization of surface and subsurface mechanical responses of nanoscale structures and the integrity of their interfaces.

(Some figures may appear in colour only in the online journal)

1. Introduction

Novel developments in material properties engineering at the nanoscale are greatly accelerated by advanced measurement methods, and particularly by scanning probe microscopy techniques that provide local property measurements at this scale. For nanoscale mechanical property characterization, the applicability and capabilities of contact resonance atomic force microscopy (CR-AFM) [1, 2] have been extensively demonstrated on a large variety of nanostructured materials [3–12]. Based on observing the change in the resonance state of an AFM probe in contact with the material investigated, the CR-AFM signal is primarily converted into

calibrated maps of elastic moduli [4, 7, 11, 13, 14]. However, when compliant materials are probed, their often attendant viscous properties can also contribute to the AFM tip-sample coupling and viscous effects become incorporated into the resonant response of the probe [3, 9, 15, 16]. In order to determine both conservative (elastic) and dissipative (viscous) material properties, CR-AFM measurement and analysis methods must be extended beyond the usual measurement of the change in resonant frequency of the AFM cantilever probe.

In this work, CR-AFM measurements were performed using a constant-excitation phase-locked-loop (PLL) detection [17] that allowed real-time monitoring of the cantilever contact resonance frequency and resonance amplitude. This

new approach enabled high spatial resolution CR-AFM measurements of intrinsic material properties, namely elastic modulus and contact damping coefficient. In addition, load-dependent CR-AFM measurements [10, 18] were used to investigate the depth dependence of the contact damping on the materials probed. By providing a subsurface mechanical characterization, the load-dependent measurements add a depth dimension to the common CR-AFM surface characterization.

The materials probed were in the form of Cu interconnects and low- k dielectric materials similar to those used currently in integrated circuits. Maps of contact resonance frequency and amplitude were used to observe the elastic and viscous surface responses with nanoscale resolution and identify heterogeneities at interfaces. The need for such investigation comes from the difficulties associated with the continuous shrinking of features in integrated circuits, for which the mechanical integrity of Cu interconnects and low- k dielectric materials raises serious challenges [19, 20]. In the past few years, various scanning probe microscopies such as ultrasonic force microscopy [21], dynamic nanoindentation [22] and ultrasound holography [23] have been used for structural defects and mechanical property characterization of integrated circuits. Quantitative nanoscale characterization of integrated Cu-low- k structures in terms of elastic modulus and contact damping coefficient by CR-AFM considerably extends these techniques [24–30].

2. Theoretical background

The mechanism of CR-AFM is relatively simple: the contact between the AFM probe and the sample is vibrated by a very small amplitude oscillation at frequencies in the kilohertz to megahertz range to detect the resonance frequencies of the system. Under such vibrations, the probe–sample contact behaves like a spring, the stiffness of which is termed the contact stiffness (refer to figure 1(a)). The probe–sample system is modeled as a beam clamped at the cantilever base and spring coupled at the other end through the contact stiffness, k^* . The key measurement in CR-AFM is to associate the change in the resonance frequency of the cantilever with the elastic modulus of the material probed. This is performed by first converting the measured resonance frequencies into contact stiffness in accordance with the model used for the dynamics of the system. Second, the contact stiffness is then converted into the elastic modulus by considering an appropriate contact model for the established contact geometry. This approach is commonly followed in CR-AFM measurements dedicated to observing the elastic response of materials.

However, besides the conservative elastic element, the probe–sample contact is characterized by a dissipative viscous element as well. To consider both of these contributions, the cantilever is modeled here as a distributed-mass Euler–Bernoulli beam and the normal probe–sample coupling as a Voigt–Kelvin element with a spring for the ideal elastic element in parallel with a dashpot (damper) for the ideal viscous element (refer to figure 1(b)) [31–33]. The

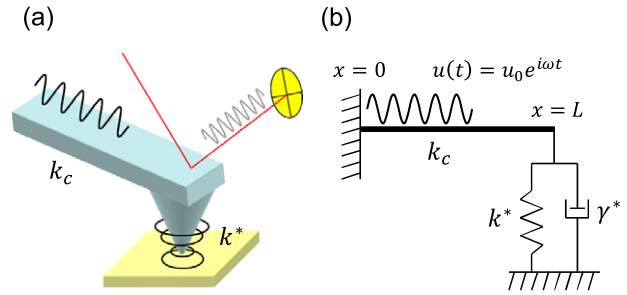


Figure 1. (a) Schematic diagram of a vibrated AFM probe brought into contact with a sample surface. The mechanical oscillations are transmitted into the sample through the spring coupling formed at the probe–sample contact. (b) Schematic representation of the probe–sample mechanical system with the representation of the contact coupling as an ideal elastic spring coupled in parallel with an ideal viscous damper.

damping response of such a vibrated system is readily obtained by characterizing the shape of its resonance peak. To determine the two parameters of interest, elastic modulus and contact damping, either the entire frequency spectrum around resonance is measured in point measurements [15, 16] or alternative pairs of two parameters (contact resonance frequency and quality factor [27] or contact resonance frequency and resonance amplitude [3]) are recorded during AFM scanning. Ultimately, these methods provide equivalent characterizations as using the contact resonance frequency and another peak parameter (the peak height for the resonance amplitude or the full width at half-height for the quality factor) enables the shape of the resonance peak to be retrieved based on the dynamics of the oscillator.

Mathematically, the elastic and viscous contact contributions are considered in the equation of the flexural vibration amplitude $y(x, t)$ along the cantilever through appropriate boundary conditions for the forces and moments at the coupling position ($x = L$ in figure 1(b)):

$$EI\partial^4 y/\partial x^4 + \eta_{\text{air}}\rho A\partial y/\partial t + \rho A\partial^2 y/\partial t^2 = 0, \quad (1)$$

with

$$y = u \quad \partial y/\partial x = 0 \quad (2)$$

at the base of the cantilever, $x = 0$ and

$$\partial^2 y/\partial x^2 = 0 \quad EI\partial^3 y/\partial x^3 = (k^*y + \gamma^*\partial y/\partial t) \quad (3)$$

at the end of the cantilever, $x = L$. In the above equations, E , I , ρ , A and k_c are the Young's modulus, cross-sectional moment of inertia, density, cross-sectional area and stiffness of the cantilever, respectively. The boundary conditions in equation (3) reflect the CR-AFM configuration used in this work, with the oscillation $u = u_0 e^{i\omega t}$ imposed on the probe–sample system from the base of the cantilever (as shown in figure 1(b)); this configuration is sometimes referred to as ultrasonic AFM [2]. In another configuration of CR-AFM known as atomic force acoustic microscopy [1], the oscillation is supplied from underneath the sample, in which case the boundary conditions are modified accordingly; a full analysis of different CR-AFM configurations can be found

in [33]. Lateral coupling was neglected in the present analysis and the tip was considered to be located at the end of the cantilever. Measurements made on the AFM probe used in this work were consistent with these assumptions.

The two quantities of interest, contact stiffness k^* and contact damping coefficient γ^* , are incorporated into the CR-AFM signal, which is filtered from the AFM displacement at the end of the cantilever [33]:

$$y_L = u_0 \frac{\alpha^3 EI (\cos \alpha L + \cosh \alpha L)}{\alpha^3 EI \Phi_1 - (k^* + i\omega\gamma^*) \Phi_2}, \quad (4)$$

where the complex wavenumber α is given by the dispersion relation

$$\alpha^4 = (\omega^2 - i\omega\eta_{\text{air}})\rho A/EI \quad (5)$$

and $\Phi_1 = 1 + \cos \alpha L \cosh \alpha L$ and $\Phi_2 = \sin \alpha L \cosh \alpha L - \cos \alpha L \sinh \alpha L$. The damping of the system has two sources: one source is the dissipation by motion of the cantilever through the air, characterized by the coefficient η_{air} (s^{-1}), and the other is the dissipation through the tip-sample coupling characterized by the contact damping coefficient γ^* (N s m^{-1}); a numerical analysis of the two damping coefficients can be found in [9]. As indicated by equation (4), the contact stiffness and contact damping regulate the amplitude of the flexural vibrations at the end of the cantilever for given working conditions, $y_L(u_0, \omega, \eta_{\text{air}}, k^*, \gamma^*)$.

The above wave equations provide the mathematical description for establishing the connection between the resonance frequencies of the cantilever and the contact stiffness in the presence of contact damping; they show how the resonance state of the cantilever is tuned according to the magnitude of the contact stiffness and damping that characterize the probe-sample contact coupling. The conversion of the contact stiffness into the elastic modulus of the material probed is thence made by means of a contact mechanics model applicable to the investigated contact geometry. With negligible adhesion forces between the AFM probe and the materials tested (as was observed for the measurements performed in this work), the contact mechanics model considered for the contact stiffness to elastic modulus conversion was the Hertz model. Thus, for the contact made between a spherical tip of radius R_T and a flat surface under an applied force F , the equation relating k^* to the reduced tip-sample elastic modulus E^* is [34]

$$k^* = (6R_T F E^*)^{1/3}. \quad (6)$$

The reduced elastic modulus E^* is given in terms of the indentation moduli of the tip, M_T , and sample, M_S :

$$1/E^* = 1/M_T + 1/M_S. \quad (7)$$

For elastically isotropic materials the indentation modulus is simply expressed in terms of the Young's modulus E and the Poisson ratio ν and $M = E/(1 - \nu^2)$. In the general case of elastically anisotropic materials, the indentation modulus can be numerically calculated along the indentation direction as a function of the elastic constants of the indented material [35].

In the context of the above mathematical formalism, the effect of contact damping on the contact resonance frequency

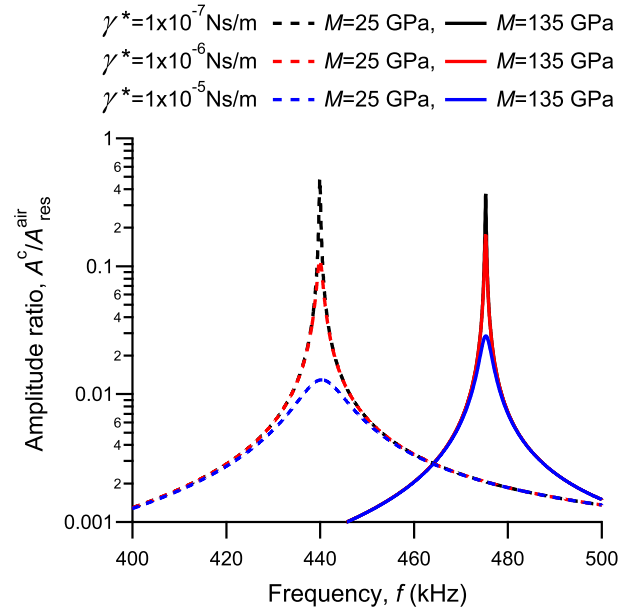


Figure 2. Damping effect on the first resonance frequency peaks of an AFM probe brought into contact with two materials of different elastic modulus: 25 GPa (dashed curves) and 135 GPa (continuous curves). For each of these materials, the change in the damping coefficient γ^* modifies the resonance peak amplitude and has no observable effect on the resonance frequency.

and resonance amplitude of the cantilever will be analyzed for materials with elastic properties similar to those probed by CR-AFM in this work. The results of such analysis will be used in a reverse procedure to convert the measured contact resonance frequencies and resonance amplitudes into the elastic moduli and damping coefficients. The effect of the contact damping on the contact resonance peak is illustrated in figure 2 for two materials of different elastic moduli, 25 GPa (comparable to that of a low- k dielectric material) and 135 GPa (as for Cu). For each of these materials, as the damping coefficient is varied over two orders of magnitude, from 1×10^{-7} to 1×10^{-5} N s m^{-1} , the contact resonance frequency (peak location) remains unchanged but the shape of the resonance peak is very sensitive to this variation. The characteristic parameters of the modeled system were as follows: cantilever stiffness $k_c = 9.5 \text{ N m}^{-1}$, first resonance in air $f_{\text{res}}^{\text{air}} = 115.1 \text{ kHz}$, $\eta_{\text{air}} = 1000 \text{ s}^{-1}$ and tip radius $R_T = 100 \text{ nm}$; the applied force at the probe-sample contact was assumed to be 150 nN. The damping effect on the resonance peak is observed in both the Q factor (the ratio of the resonance frequency and the full width at half-height of the resonance peak) and resonance amplitude A_{res}^c : as the damping coefficient is increased the resonance peaks become broader (smaller Q factor) and shorter (smaller A_{res}^c). For a given oscillator, the quantities Q factor and A_{res}^c are interdependent descriptions of the dissipation processes occurring within the oscillator. Either of them can be used in data analysis depending on the practical convenience in measurements. In the following, the analysis will be made in terms of A_{res}^c , as this is an experimental parameter that can be accessed directly in CR-AFM operated in constant-excitation PLL modulation

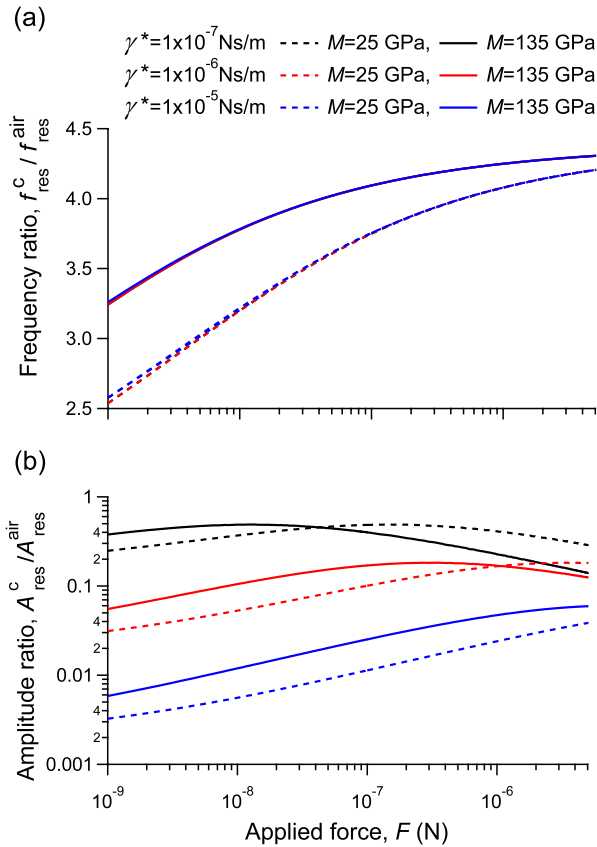


Figure 3. For two materials of different elastic modulus, 25 GPa (dashed curves) and 135 GPa (continuous curves), the contact force dependences of (a) the resonance frequency and (b) resonance amplitude of the first contact mode are plotted for various contact damping coefficients. The frequencies are normalized to the first resonance frequency of the cantilever in air and the amplitudes to the resonance amplitude of the first resonance peak in air.

as in this work; in constant-excitation PLL modulation [36] the excitation amplitude of the cantilever is kept constant while the phase shift between the driving and response signals is used to track the change in the resonance frequency of the cantilever. Both the contact resonance frequency f_{res}^c and resonance amplitude A_{res}^c used herein characterize the first contact oscillation mode of the clamped-spring-coupled cantilever.

The invariance of the contact resonance frequency with damping is illustrated in the plots of figure 3(a) over the nanonewton to micronewton range of the applied forces for both materials considered; the contact resonance frequency versus applied force response is specific to a given material but is not affected by the change in contact damping. This means that, in most cases, contact resonance frequency measurements are sufficient in CR-AFM investigations concerned only with determination of the elastic response of materials. However, the applied force dependence of A_{res}^c over the same force range exhibits a characteristic response to contact damping. Unlike the Q factor (not shown here), which depends monotonically on the contact stiffness, A_{res}^c does not vary monotonically with the contact stiffness (or the applied force as shown in figure 3(b)) but exhibits a maximum,

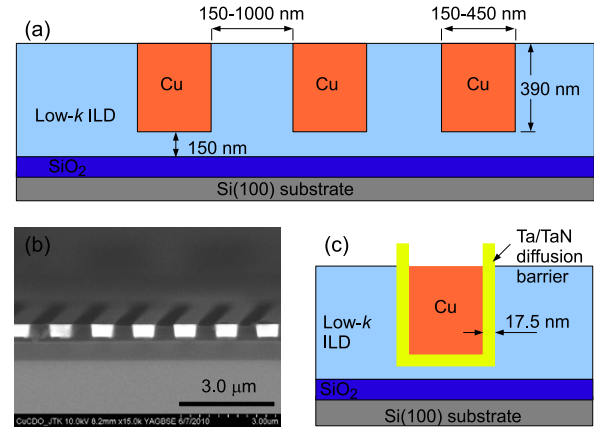


Figure 4. (a) Schematic and (b) scanning electron microscopy image of Cu lines inlaid in a low- k interlayer dielectric. (c) The separation between each Cu line and its surrounding dielectric is made through a Ta/TaN diffusion barrier about 18 nm in thickness.

characteristic for a given contact damping. For a given contact stiffness (or applied force), A_{res}^c still varies monotonically with the contact damping; the amplitude increases with the decrease in contact damping. The analysis becomes a little bit more complicated when two different materials are probed (e.g. test and reference materials in CR-AFM) because for two different contact stiffnesses the amplitudes and contact damping will not be necessary in a proportional relationship. As can be observed in figure 3(b), the amplitude contrast between the two materials with elastic moduli of 25 and 135 GPa could change as a function of the applied force: for contact damping of 1×10^{-5} N s m⁻¹, the amplitude is larger on the stiffer material over the entire considered force range. However, at smaller contact damping, the amplitude is larger on the stiffer material only at small applied forces and becomes smaller on the stiffer material at larger applied forces. This peculiar relationship between the resonance amplitude and contact damping needs to be considered for a correct evaluation of the contact damping from CR-AFM measurements made at a given applied contact force.

An equivalent analysis of the dynamics of the spring-coupled cantilever was performed in [16] to relate the contact stiffness to the quality factor of the second and third vibration modes; the relationship between resonance amplitude and contact damping (the resonance amplitude increases with the applied force) can also be observed for the few frequency spectra shown.

3. Experimental measurements

The sample investigated in this work consisted of Cu lines inlaid in a low- k interlayer dielectric, as used in microelectronic devices [37]. After the low- k dielectric film was deposited on a Si substrate with an overlying SiO₂ film, the low- k film underwent several plasma etches, cleans and polishing steps to fabricate the Cu lines. In figure 4, the cross section and the upper surface of the sample are shown in schematic representations as well as a scanning

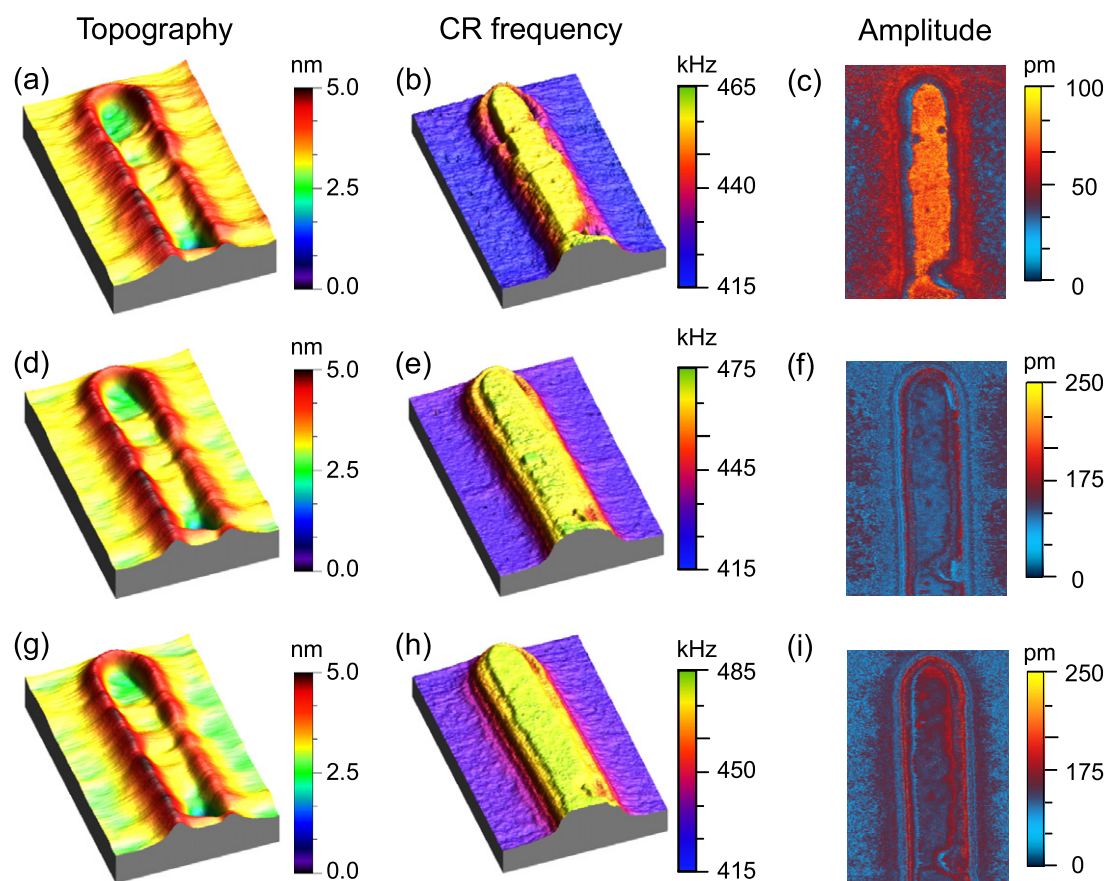


Figure 5. Topography ((a), (d) and (g)), contact resonance frequency ((b), (e) and (h)) and resonance amplitude ((c), (f) and (i)) maps recorded during CR-AFM scans at various loads: 50 nN ((a)–(c)), 110 nN ((d)–(f)) and 215 nN ((g)–(i)). The scan area was $650 \text{ nm} \times 1000 \text{ nm}$. The topography and contact resonance maps are shown in three-dimensional views and the resonance amplitude maps in two-dimensional views.

electron microscopy image. The Cu lines are separated from the dielectric by a tantalum nitride/tantalum (TaN/Ta) diffusion barrier, which was about 18 nm in width and stood a few nanometers above the dielectric surface. The local variations in topography and materials of the sample provide an excellent test vehicle for the CR-AFM capabilities of mapping and identifying the nanoscale mechanical response in terms of elastic modulus and contact damping.

In the present work, the detection of the contact resonance frequency and resonance amplitude during regular contact-mode AFM scans was performed by using a SPECS Zurich GmbH PLL controller (Zurich, Switzerland) operated in constant-excitation mode. The PLL controller was connected through a signal access module to a MultiMode V Veeco/Bruker scanning probe microscope (Santa Barbara, CA, USA)³ and the measured resonance frequency and amplitude were fed directly into the external channels of the AFM controller for real-time imaging during scanning. The

AFM probe used for CR-AFM mapping was a PPP-SEIH integrated Si probe (NanoSensors, Neuchatel, Switzerland) (see footnote 3) with a cantilever spring constant of $9.5 \pm 0.2 \text{ N m}^{-1}$ (measured by using the integrated thermal-noise calibration method of the scanning probe microscope) and the first two free resonance frequencies of 115.5 kHz and 721.3 kHz, respectively. From the measurement of the first two contact resonance frequencies at a few applied forces, the tip position along the cantilever was calculated to be within 0.3% of the end of the cantilever. All uncertainties quoted in this work represent the standard deviations of repeated measurements.

CR-AFM maps of $650 \text{ nm} \times 1000 \text{ nm}$ ($332 \text{ pixels} \times 512 \text{ pixels}$) encompassing the end of a Cu line are shown in figure 5 in the form of topography, contact resonance frequency and resonance amplitude at three different applied loads: 50, 110 and 215 nN. The topography images are shown in the first column of figure 5 as acquired in contact mode during CR-AFM and the contact resonance frequency and resonance amplitude maps are shown in the second and third columns of figure 5 as retrieved from the PLL signals. While the imaged topography was the same at each applied force, substantial differences are observed in both the contact resonance frequency and amplitude maps as the

³ Certain commercial equipment, instruments or materials are identified in this document. Such identification does not imply recommendation or endorsement by the National Institute of Standards and Technology, nor does it imply that the products identified are necessarily the best available for the purpose.

applied force was varied. As the applied force was increased, the contact resonance frequencies on both the Cu line and the surrounding dielectric increased (different scale bars were used in figures 5(b), (e) and (h)). However, inspection of the amplitude contrast reveals that a larger amplitude on Cu than on the dielectric was observed at 50 nN whereas at greater loads this contrast almost vanishes. The TaN/Ta diffusion barrier is clearly visible in each image: in the topography the barrier stands a few nanometers above the surface plane; in the contact resonance frequency the barrier has a contrast intermediate to that of the Cu and low- k dielectric material; and in the resonance amplitude maps an inversion in the contrast for the barrier can be observed, passing from a smaller amplitude at 50 nN to a larger amplitude at 215 nN. A few structural defects in the Cu line (two dots close to the top end and a more extended feature at the bottom) are observed in the contact resonance frequency and resonance amplitude maps with greater contrast at smaller applied forces where the contact radius was reduced. As the contact radius was increased with the increase in the applied force (from top to bottom in figure 5), the contrast around these defects progressively vanished.

Individual profiles across the imaged Cu line are shown in figure 6. In the topographic profile (figure 6(a)) the AFM tip introduced significant dilation effects around the walls of the TaN/Ta diffusion barrier. The passage of the tip over the barrier is clearly observed also in the contact resonance frequency and amplitude profiles. As the barrier stands above the rest of the surface, the contact geometry changes dramatically over the edge, so a clear conversion of the measured contact resonance frequency into the elastic modulus of this barrier is difficult as the contact area change during passage over the barrier is required. At each applied force, clear plateaus in the contact resonance frequency over the Cu line are observed, most likely when the tip was not in contact with any of the delimiting edge barriers. The edges are also marked clearly in the resonance amplitude profiles. At 50 nN, the amplitude on the Cu line is greater than on the dielectric and the barrier. However, at greater applied forces, the amplitude contrast changed such that the resonance amplitude was greater on the TaN/Ta barriers than on the Cu and low- k dielectric material. As described in section 2, to interpret this amplitude contrast as a function of applied force, the dynamics of the probe-sample system needs to be properly considered as a function of the applied load.

4. Results and discussion

Besides the above qualitative statements, the contact resonance frequency and resonance amplitude maps can also be analyzed quantitatively. Moreover, by performing CR-AFM at different applied forces (or equivalently different indentation depths), possible depth-dependent inhomogeneities in the elastic and viscous response of materials can be revealed. Thus, the contact resonance frequency scans shown in figures 5(b), (e) and (h) provided the average contact resonance frequencies on Cu and low- k

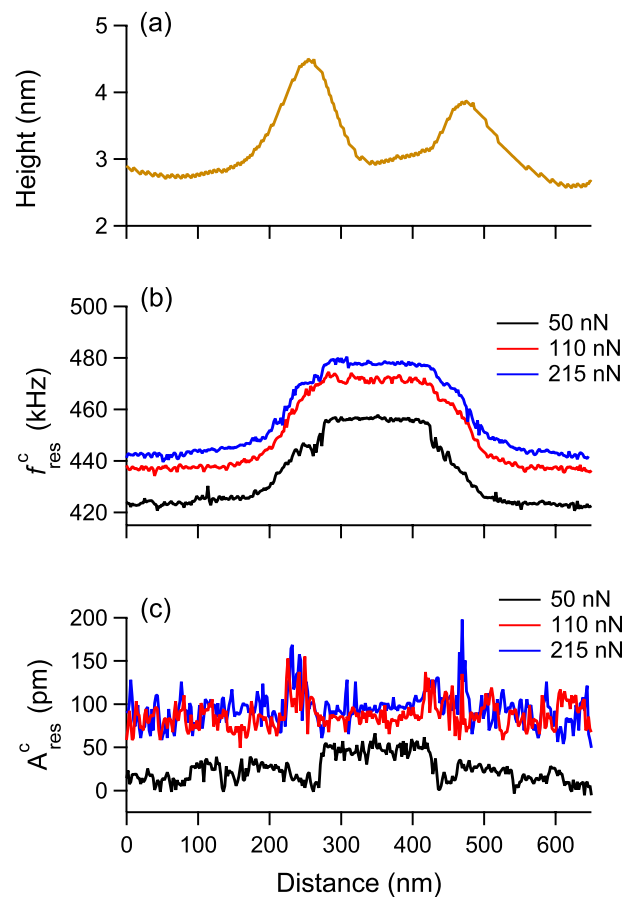


Figure 6. Cross-section profiles of the maps shown in figure 5: (a) topography, (b) contact resonance frequency and (c) resonance amplitude at various applied forces.

dielectric material at three different applied forces. These average values were used to adjust the fitted curves of the contact resonance frequency versus applied force shown in figure 7 for each material. By determining the indentation moduli from CR-AFM maps at a few different applied forces rather than from point measurements or maps at a single given applied force, the measurement uncertainty is greatly reduced [18]. In the case of Cu, the fitted curve was calculated by considering the tip radius as a fitting parameter and using 165 and 135 GPa for the indentation moduli of Si and Cu; the best fit was provided by an R_T of (100 ± 20) nm. With this value for the tip radius, the contact resonance frequency versus applied force dependence for the low- k dielectric material was best fitted by an indentation modulus of (25 ± 3) GPa. The uncertainties generated by the tip radius estimation in the calculated fitting dependences for the average contact resonance frequency versus the applied force of the two materials are shown in figure 7. In a previous work [18] it has been found that the elastic modulus of the same low- k dielectric material in the form of an unpatterned pristine film was around 10–12 GPa. This pronounced stiffness enhancement indicates a change in the elastic properties of the low- k dielectric material during its patterning into forming the lines. It is conceivable that

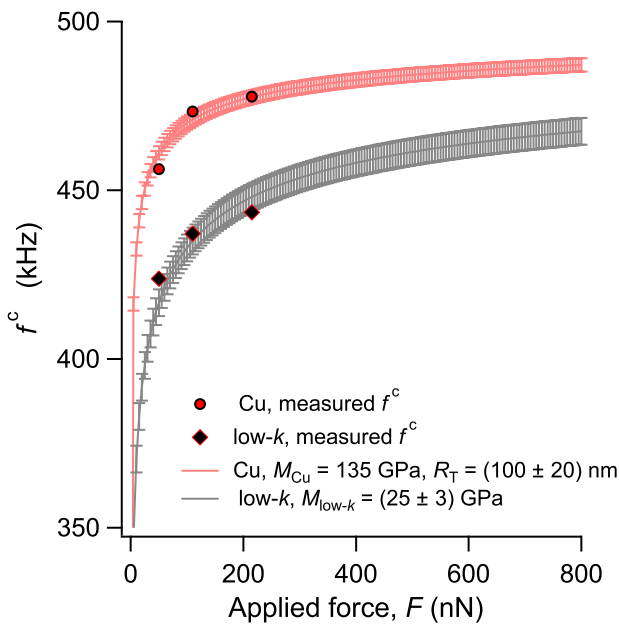


Figure 7. Average values of the contact resonance frequencies on Cu and low- k dielectric material from the maps shown in figures 5(b), (e) and (h) at three different applied forces; the standard deviations of these average frequencies were within 2 kHz, which is about the size of the symbols. The force dependences of the measured contact resonance frequencies were used as fitting constraints for the indentation moduli of the reference (Cu) and test (low- k dielectric) materials. The data scattering around each calculated curve was considered by an uncertainty of 20 nm in the estimated radius of the AFM probe.

structural densification via plasma treatment could induce not only a material stiffening but also an increase in the dielectric constant of low- k materials during processing.

Using the determined elastic moduli, the average values of the resonance amplitudes measured at 50, 110 and 215 nN (refer to figures 5(c), (f) and (i)) were used to determine the contact damping coefficients of the two materials. However, no single contact damping coefficient was found to provide a good fit for either Cu or low- k dielectric material. Instead, the pronounced variations in the resonance amplitudes at the forces applied in measurements indicated a possible depth dependence for the contact damping, with a decay in the contact damping below the surface. To further investigate this behavior, load-dependent CR-AFM point measurements were performed at separate locations on Cu and low- k dielectric material, with the resonance amplitude recorded continuously as the AFM probe was brought into and out of contact with the sample.

Examples of force and resonance amplitude responses during approach and retract force–displacement measurements at locations on Cu and low- k dielectric material are shown in figure 8. The PLL frequency bandwidth was adjusted only for contact resonance detection, which allowed resonance tracking only in contact and not out of contact; the amplitudes in figures 8(a) and (b) are resonance amplitudes only during contact. From the examples shown in figure 8, it can be observed that, for the range of the applied forces used, the resonance amplitude on the dielectric increased continuously as the applied force was increased and the resonance amplitude on the Cu first increased with the applied force and then decreased. These characteristic responses were consistently obtained in alternating measurements on the two materials. Such dependences were observed in the theoretical analysis discussed in section 2 but no good fits would be obtained here if a constant contact damping coefficient is assumed for each material. Instead, these load dependences

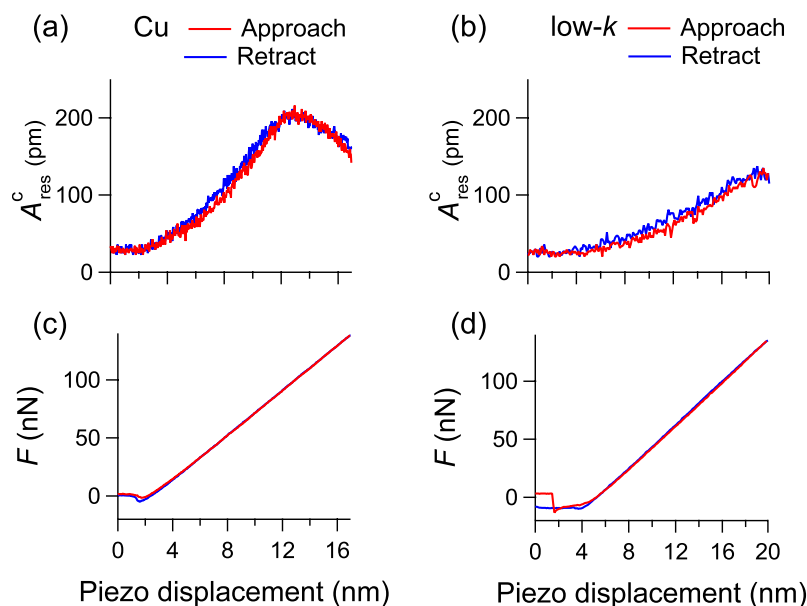


Figure 8. (a) and (b) Resonance amplitude and (c) and (d) force versus piezo-displacement during approach and retract excursions of the AFM probe on Cu and low- k dielectric material.

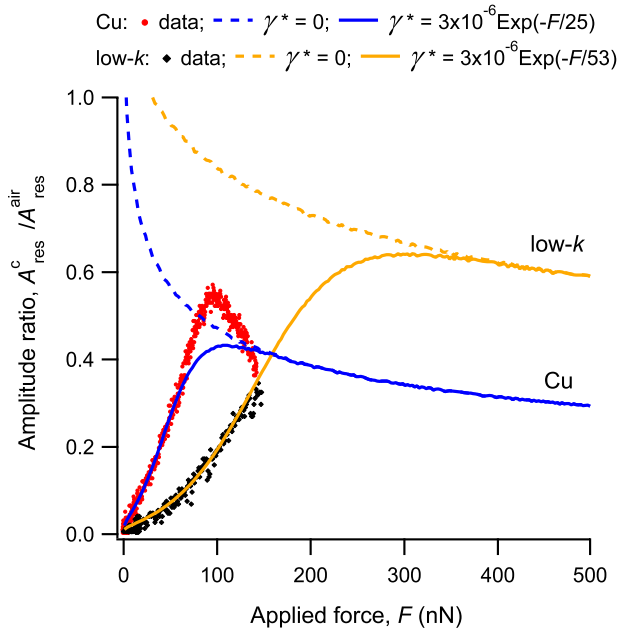


Figure 9. Measurements and theoretical curves for the resonance amplitude on Cu and low-*k* dielectric materials. The experimental values were extracted from load-dependent CR-AFM measurements and the fits (continuous lines) were calculated by considering an exponential depth decay of the damping coefficient as an adjustable parameter for each material. In contrast with the case of contact damping, the resonance amplitude would decay monotonically with increasing applied force when no contact damping is present (dashed line).

exhibited by the resonance amplitudes were retrieved when an exponential decay for the contact damping coefficient γ^* as a function of the applied force F (or equivalently the elastic deformation d) was considered:

$$\gamma^* = \gamma_0^* \exp[-F/F_0] = \gamma_0^* \exp[-(d/d_0)^{3/2}], \quad (8)$$

where the parameters F_0 and d_0 represent the force and deformation decay constants, respectively; γ_0^* stands for the surface contact damping coefficient. Such dependences for the contact damping coefficients were considered in calculating the fitted curves shown in figure 9 for the resonance amplitude versus applied force measurements, with a different decay constant in the contact damping coefficient for each material. It can be observed that, as the applied force increases, the effect of contact damping on the resonance amplitude diminishes and the theoretical curves of the resonance amplitude with and without contact damping overlap each other. This means that, in the limit of large applied forces, the viscous dissipation diminishes and the coupling becomes essentially elastic (assuming that the elastic regime is still valid at such large applied forces).

The proposed depth-dependent behavior for the damping coefficient reproduced very well the measured damped resonance amplitudes as a function of the applied force, on the low-*k* dielectric material up to forces of 150 nN and on Cu up to forces of 50 nN. Although the quantitative agreement is less accurate for Cu at applied forces greater than 50 nN, the qualitative dependence captures realistically the contact damping response on this material; the measurements indicate a much more pronounced damping on Cu than that considered by the exponential decay. In other words, the contact damping decays more slowly with applied force on the low-*k* dielectric material than on Cu. However, the damping is observed to be similar in both materials at the surface and this can be rationalized with the observation that right at the surface the main contribution could come from adhesion. As can be observed in the force–displacement measurements, the adhesive forces for both materials are comparable. In figure 10 the calculated subsurface decays of the contact damping coefficients are shown for the two materials as functions of applied force and deformation. From figure 10(a), it can be observed that, at a given applied force, a stronger

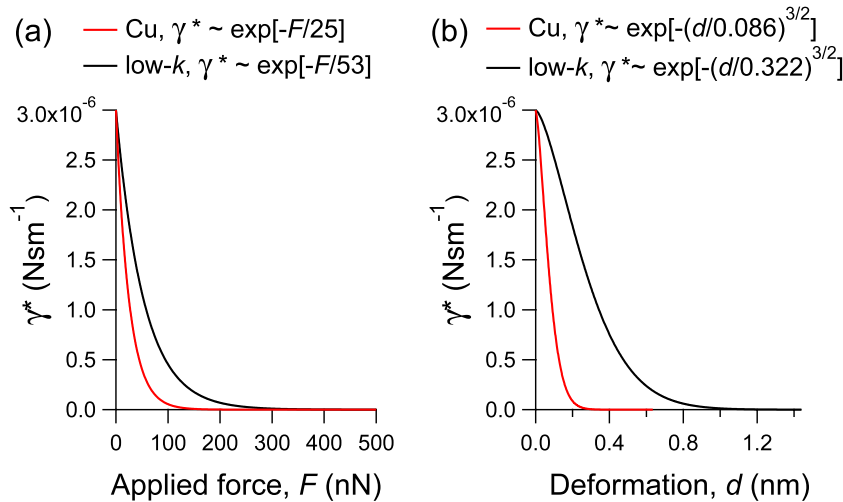


Figure 10. (a) and (b) The applied force and depth-dependent exponential decays of the contact damping coefficients of Cu and low-*k* dielectric materials. The curves were calculated from the fits shown in figure 9 and underestimate the damping attenuation on Cu at applied forces larger than 50 nN.

damping occurs on the low- k dielectric material than on Cu, e.g. the attenuation ratio between the two materials is about 3 at an applied force of 50 nN and about 8 at an applied force of 100 nN (and is even greater, considering that the assumed exponential decay for the depth dependence of the damping coefficient underestimates the measurements). From the depth dependences of the damping coefficients shown in figure 10(b), it can be judged that the same contact damping is associated with larger deformations on the low- k material than on Cu, e.g. a 1×10^{-6} N s m $^{-1}$ damping coefficient corresponds to a deformation about four times larger on the low- k material than on Cu. A negligible contact damping on Cu will be within a quarter of a nanometer and on the low- k material the attenuation of the contact damping will occur for deformations of the order of a nanometer.

5. Summary

The conservative (elastic modulus) and dissipative (contact damping) contributions to CR-AFM measurements on integrated Cu-low- k structures were resolved in this study. The measurement analysis was based on two measurable quantities, the contact resonance frequency and the resonance amplitude. For the elastic and viscous properties of the materials investigated, it was found that the contact resonance frequency depends almost entirely on the elastic modulus. However, the resonance amplitude is a function of both the elastic modulus and contact damping. Thus, by measuring both the contact resonance frequency and the resonance amplitude, as in the example shown for integrated Cu-low- k structures, the contact damping response of materials probed can be retrieved. From single-point CR-AFM measurements made at shallow depth indentations, the resonance amplitude response of the materials revealed a depth dependence of the contact damping. The superficial contact damping was found to persist in nanometer-size deformations of the low- k dielectric material and was significantly attenuated in the Cu. The depth decay of the contact damping of these two materials is inversely correlated with their stiffness. By providing simultaneous elastic modulus and contact damping measurements, the CR-AFM methodology used here adds new capabilities to the existing AFM-based techniques dedicated to mapping the viscoelastic mechanical response of materials at the nanoscale.

References

- [1] Rabe U, Janser K and Arnold W 1996 *Rev. Sci. Instrum.* **67** 3281
- [2] Yamanaka K and Nakano S 1996 *Japan. J. Appl. Phys.* **35** 3787
- [3] Yamanaka K, Maruyama Y, Tsuji T and Nakamoto K 2001 *Appl. Phys. Lett.* **78** 1939
- [4] Passeri D, Bettucci A, Germano M, Rossi M, Alippi A, Sessa V, Fiori A, Tamburri E and Terranova M L 2006 *Appl. Phys. Lett.* **88** 121910
- [5] Hurley D C, Kopycinska-Muller M, Langlois E D, Kos A B and Barbosa N 2006 *Appl. Phys. Lett.* **89** 021911
- [6] Stan G, Ciobanu C V, Parthangal P M and Cook R F 2007 *Nano Lett.* **7** 3691
- [7] Kumar A, Rabe U, Hirsekorn S and Arnold W 2008 *Appl. Phys. Lett.* **92** 183106
- [8] Stan G, Ciobanu C V, Thayer T P, Wang G T, Creighton J R, Purushotham K P, Bendersky L A and Cook R F 2009 *Nanotechnology* **20** 035706
- [9] Caron A and Arnold W 2009 *Acta Mater.* **57** 4353
- [10] Stan G, Krylyuk S, Davydov A V and Cook R F 2010 *Nano Lett.* **10** 2031
- [11] Nair S S, Wang S and Hurley D C 2010 *Composites A* **41** 624
- [12] Nikiforov M P, Thompson G L, Reukov V V, Jesse S, Guo S, Rodriguez B J, Seal K, Vertegel A A and Kalinin S V 2010 *ACS Nano* **4** 689
- [13] Hurley D C, Kopycinska-Mueller M, Kos A B and Geiss R H 2005 *Meas. Sci. Technol.* **16** 2167
- [14] Stan G and Cook R F 2008 *Nanotechnology* **19** 235701
- [15] Yuya P A, Hurley D C and Turner J A 2008 *J. Appl. Phys.* **104** 074916
- [16] Yuya P A, Hurley D C and Turner J A 2011 *J. Appl. Phys.* **109** 113528
- [17] Kobayashi K, Yamada H and Matsushige K 2002 *Surf. Interface Anal.* **33** 89
- [18] Stan G, King S W and Cook R F 2009 *J. Mater. Sci.* **24** 2960
- [19] Zschech E, Huebner R, Potapov P, Zienert I, Meyer M A, Chumakov D, Geisler H, Hecker M, Engelmann H J and Langer E 2008 *Proc. IEEE 2008 Int. Interconnect Technol. Conf.* p 67
- [20] Chen F and Shinosky M 2009 *IEEE Trans. Electron Dev.* **56** 2
- [21] Muthuswami L and Geer R E 2004 *Appl. Phys. Lett.* **84** 5082
- [22] Jiang L, Geisler H and Zschech E 2006 *Thin Solid Films* **515** 2230
- [23] Gajendra Shekhawat G, Srivastava A, Avasthy S and Dravid V 2009 *Appl. Phys. Lett.* **95** 263101
- [24] Gotsmann B, Seidel C, Anczykowski B and Fuchs H 1999 *Phys. Rev. B* **60** 11051
- [25] Hölscher H, Gotsmann B, Allers W, Schwarz U D, Fuchs H and Wiesendanger R 2001 *Phys. Rev. B* **64** 075402
- [26] Martinez N F and Garcia R 2006 *Nanotechnology* **17** S167
- [27] Jesse S, Kalinin S V, Proksch R, Baddorf A P and Rodriguez B J 2007 *Nanotechnology* **18** 435503
- [28] Sahin O, Magonov S, Su S, Quate C F and Solgaard O 2007 *Nature Nanotechnol.* **2** 507
- [29] Chawla G and Solares S D 2011 *Appl. Phys. Lett.* **99** 074103
- [30] Gannepalli A, Yablon D G, Tsou A H and Proksch R 2011 *Nanotechnology* **22** 355705
- [31] Wright O and Nishiguchi N 1997 *Appl. Phys. Lett.* **71** 626
- [32] Turner J A, Hirsekorn S, Rabe U and Arnold W 1997 *J. Appl. Phys.* **82** 966
- [33] Rabe U 2006 *Applied Scanning Probe Microscopy* vol II, ed B Bhushan and H Fuchs (Berlin: Springer) p 3790
- [34] Johnson K L 1985 *Contact Mechanics* (Cambridge: Cambridge University Press)
- [35] Vlassak J J and Nix W D 1993 *Phil. Mag. A* **67** 1045
- [36] Hölscher H, Gotsmann B and Schirmeisen A 2003 *Phys. Rev. B* **68** 153401
- [37] Jan C-H et al 2003 *Proc. IEEE Int. Interconnect Technology Conf. (Burlingame, CA, June 2003)* p 15